

Cite this: *J. Mater. Chem. A*, 2014, 2, 7373

Rambutan-like Ni/MWCNT heterostructures: Easy synthesis, formation mechanism, and controlled static magnetic and microwave electromagnetic characteristics†

Guoxiu Tong,^{*a} Fangting Liu,^a Wenhua Wu,^a Fangfang Du^a and Jianguo Guan^b

Rambutan-like heterostructures consisting of Ni microspheres coated with oriented multiwall carbon nanotubes (MWCNTs) were synthesized by the one-pot thermal decomposition of a mixture of organic matter and Ni precursors. X-ray diffraction, scanning electron microscopy, transmission electron microscopy, and Raman spectroscopy were used to reveal the formation mechanism. The growth of MWCNTs capped by Ni nanoparticles on the surface of the Ni nanoparticle-built microspheres followed a tip-growth mode. The composition and morphology of the rambutan-like heterostructures were easily controlled by changing the reaction time, mass ratio δ of polyethylene glycol (PEG) 20 000 to NiO, as well as type of C source and Ni precursor. Increasing the δ favored not only the increased C mass fraction but also the morphological conversion from Ni/C film core-shell structures to rambutan-like Ni/MWCNT heterostructures. Such changes caused the decreased saturation magnetization and enhanced permittivity properties with δ . Owing to intensive eddy current loss and multiresonance behaviors, rambutan-like Ni/MWCNT heterostructures with long MWCNTs exhibited significantly improved complex permeability and magnetic loss. Ni/MWCNT heterostructures coated by short MWCNTs showed an optimal microwave absorption property with a minimum R_L value of -37.9 dB occurring at 12.8 GHz. This work provides effective guidelines for devising and synthesizing highly efficient microwave-absorbing materials.

Received 8th January 2014
Accepted 21st February 2014

DOI: 10.1039/c4ta00117f

www.rsc.org/MaterialsA

Introduction

Hybrid nanomaterials containing carbon nanotubes (CNTs) are attracting considerable attention because of their numerous unique properties and multifunctions different from pure CNTs. For example, Fe powders modified by adding a small quantity of CNTs can produce materials that can absorb electromagnetic (EM) waves. These materials are more highly absorptive, thinner, and lighter than pure CNTs and Fe powders because of significantly improved EM matching and absorption performances.¹ Ni catalysts dispersed on multiwall CNT (MWCNT) surfaces can effectively dissociate hydrogen molecules in the gas phase, thereby providing an effective reversible

hydrogen storage method.² Composites of MWCNTs and Ni as electrodes reportedly show higher discharge capacitance because of enhanced electrochemical activity.³ Furthermore, CNT-supported Ni composites show excellent electrocatalytic activity for ethanol oxidation in alkaline solution.⁴ Interestingly, the above properties can be controlled by tuning the composition, size, and spatial orientation of CNTs.

Various CNT-based hybrid structures have been designed and prepared, including encapsulation of CNTs with metal,⁵ metal oxide, and organic matter; filling of CNTs with nanoclusters (Co,⁶ Fe,⁷ Ni,⁸ FeNi,⁹ Fe₃Co_{1-x},¹⁰ and Cu₂O,¹¹ etc.); as well as blending compound of CNTs and Fe,¹ CNT/CNF hierarchical structure,¹² flower-like structures,¹³⁻¹⁵ and pillaring graphene oxide with CNTs.¹⁶ The formation of CNT-based hybrid structures can be achieved by arc discharge, laser ablation, gas-phase catalytic growth, and chemical vapor deposition (CVD) methods.¹⁷

Our group has chosen to study rambutan-like Ni/MWCNT heterostructures because of their novel properties and promising applications in biomedicine, energy storage, photocatalysis, microwave absorption, and nanodevices. In particular, the composition and shape control over rambutan-like Ni/MWCNT heterostructures is expected to modulate the

^aCollege of Chemistry and Life Sciences, Zhejiang Normal University, Jinhua 321004, People's Republic of China. E-mail: tonggx@zjnu.cn; Fax: +86-579-82282269; Tel: +86-579-82282269

^bState Key Laboratory of Advanced Technology for Materials Synthesis and Processing, Wuhan University of Technology, Wuhan 437000, People's Republic of China

† Electronic supplementary information (ESI) available: SEM images of the product obtained produced from different Ni sources and frequency dependence of the complex permittivity and permeability of wax composites containing various mass fractions of the typical product. See DOI: 10.1039/c4ta00117f

microwave electromagnetic properties and to generate novel absorbing mechanism. Despite their fundamental and technological importance, the challenge of synthetically and systematically controlling the compositions and morphology of rambutan-like CNT-based hybrid structures has been met with limited success.^{13–15} Zheng *et al.*¹³ obtained Co flowers coated with open-tipped MWCNTs by the simple Co powder catalytic pyrolysis of acetone in a stainless-steel autoclave at 550 °C for 12 h. Han *et al.*¹⁵ synthesized a composite structure consisting of hollow Ni microspheres coated with oriented CNTs by the CVD of acetylene at 800 °C under catalysis of hollow Ni particle-built microspheres. Moreover, the reported literature is few on studies of the relationship between the structure and the microwave absorption properties.

In this study, we developed a general catalytic CVD method to selectively prepare rambutan-like Ni/MWCNT heterostructures with tunable morphology and composition. Compared with previous reports,^{13–15} high yields of rambutan-like Ni/MWCNT heterostructures were obtained using organic matter [polyethylene glycol (PEG) 400–20 000, paraffin, and benzene] instead of acetone and acetylene as the C source, as well as Ni-based composites instead of Ni particles as Ni sources and catalysts. Use of such materials will open a new way in the synthesis of CNT-based hybrid materials. Furthermore, the static magnetic and microwave electromagnetic characteristics of rambutan-like Ni/MWCNT heterostructures were systematically investigated.

Experimental

Preparation

All chemical reagents were from Shanghai Chemical Reagents Company. They were of analytical grade and used as received without any further purification. In a typical synthesis, 0.2 g of NiO powder and 1.5 g of PEG 20 000 were ultrasonically dispersed with 5 mL of acetone. After acetone was evaporated, the mixture described above was loaded with a ceramic vessel (1.2 cm × 9.0 cm × 1.0 cm) and placed in a horizontal tube furnace. Under Ar protection, the furnace temperature was increased from room temperature to 750 °C for 30 min and kept at 750 °C for 2 h. Finally, the system was allowed to cool to room temperature under N₂. A black solid product was deposited at the bottom of the vessel, indicating the formation of rambutan-like Ni/MWCNT heterostructures. The gas flow rate was 1.0 L min^{−1}. NiO octahedral powders were prepared by nickel nitrate thermal decomposition as previously described.¹⁸

Morphology and composite control over the obtained products were further analyzed by altering the experimental conditions, including the mass ratio of PEG 20 000 to NiO ($\delta = 3.0, 7.5, 15, \text{ and } 50$), reaction time ($t = 0.5, 1, 2, \text{ and } 4 \text{ h}$), Ni source [NiO and Ni(OH)₂], and C source (PEG 400–20 000, paraffin, benzene, *etc.*).

Characterization

Powder X-ray diffraction (XRD) patterns were recorded on a D/Max-RB X-ray diffractometer (Rigaku, Japan), using CuK α

radiation at a scan rate of 0.05° 2 θ s^{−1}. The element composition of the samples was characterized by an energy dispersive X-ray spectrometer (EDX, EX-250, Horiba, Japan) operated at 20.0 kV, attached on a Hitachi S-4800 field-emission scanning electron microscope. The Raman spectrum of the sample was taken at room temperature on a SPEX 1403 spectrometer with an argon-ion laser at an excitation wavelength of 514.5 nm. Scanning electron microscopy (SEM) image was observed on an S-4800 Field Emission SEM (FESEM, Hitachi, Japan) at an accelerating voltage of 10 kV. High-resolution transmission electron microscopy (HRTEM) images were captured on a JEM 2100F microscope at an accelerating voltage of 200 kV.

Measurement of properties

The static magnetic properties were measured by a vibrating-sample magnetometer (4HF; ADE, Chicago, IL) at room temperature. The coaxial line method was applied to determine the relative complex permeability and permittivity of the sample-wax composites through an Agilent N5230 vector network analyzer system. The cylindrical toroidal samples with 3.0 mm in inner diameter, 7.0 mm in outer diameter and a thickness of *ca.* 3.0 mm were fabricated by uniformly mixing wax with the absorbents in a mass ratio of 30% and then pressed into cylindrical compacts.

Results and discussion

Synthesis and characterization of the typical product

The crystalline structure, composition, and morphology of the typical pyrolysis product were analyzed by XRD, EDX, Raman spectroscopy, SEM, and TEM. The XRD data in Fig. 1a show some peaks marked by ♥ that could be identified as hexagonal graphite (JCPDS card no. 41-1487); the others marked by ♣ were perfectly similar to those in face-centered-cubic (FCC) Ni standard card (JCPDS card no. 65-2865). Therefore, the obtained products were mixtures of FCC Ni and hexagonal graphite. No impurities such as NiO and NiC_x were detected. This result suggests that NiO was completely reduced and that the catalyst was not NiC_x. No shift in the peak positions of Ni compared to the Ni standard pattern indicated that no C atoms inserted inside the nickel lattice.¹⁹ The stronger diffraction peak relative to the (111) facet rather than to other planes demonstrated that Ni nanocrystals preferentially grew along the [111] direction. This phenomenon can be interpreted by two primary factors.

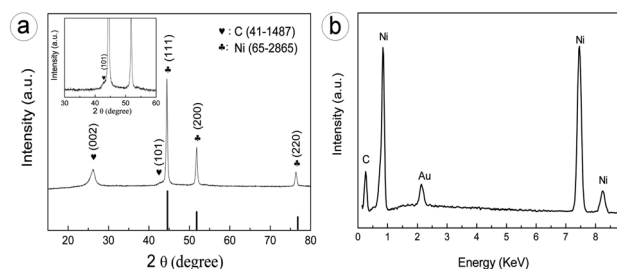


Fig. 1 (a) XRD pattern and (b) EDX spectrum of the typical product.

One is the surface-energy general sequence for the FCC structure that Ni may hold, $\gamma(111) < \gamma(100) < \gamma(110)$.²⁰ The other is an easy axis along the $[111]$ direction for single-crystal Ni.¹⁸ Apparently, this preferential growth $[111]$ direction for Ni subunits was governed by the principles of minimum magnetic anisotropic energy and minimum surface free energy. The (111) boundary crystal planes of the included metals normally facilitated organic molecule absorption during C deposition, due to their thermodynamic stability.^{21,22} C migration onto the subsurface was actually favored for both Ni(111) and Ni(100).¹⁹ The energy barriers of Ni(111) and Ni(100) were 1.92 and 1.45 eV, respectively, which were relatively high values. However, each C atom gained 0.3 eV by subsurface diffusion. Thus, we speculated that CNTs attached onto the surface of Ni particles grew by incorporating C atoms provided through (111) subsurface diffusion. The broadened and weak peak relative to hexagonal graphite can be attributed to the low content or low crystallinity of the hexagonal graphite of the product. EDX analysis of the typical product further confirmed that only Ni and C elements coexisted in the samples (Fig. 1b), and the Ni and C mass fractions were 66.33% and 33.67%, respectively.

Further information on the C structure was obtained by Raman investigation, as shown in Fig. 2. The Raman scattering spectrum of the typical product was in accordance with the MWCNT feature.²³ Both D band at 1344 cm^{-1} and G band at 1586 cm^{-1} came from first-order Raman scattering. The former is usually related to lattice disorders in the sp^2 -hybridized C atoms and/or amorphous C deposits, whereas the latter is ascribed to the highly oriented sp^2 hexagonal graphitic lattice.^{15,24} Other bands situated at 2685 and 2935 cm^{-1} originated from the second-order Raman scattering. The D band was stronger than the G band because of the large I_D/I_G ratio (1.256), indicating that the produced CNTs had high defect level or low degree of graphitization in the atomic C structure. In addition, no peak was found in the low-frequency domain.²⁵ Therefore, no single-wall CNTs were present in the composite structures. The above results are consistent with the XRD pattern and the subsequent HRTEM results.

SEM observations revealed that a typical product consisted of a large number of uniform rambutan-like architectures about 1 to 2 μm in size (Fig. 3a). A typical particle presented a core-shell structure (Fig. 3b and c). The core was built from many nanoparticles, whereas the shell was constructed by numerous

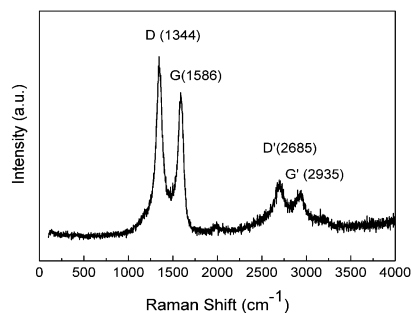


Fig. 2 Raman spectrum of the typical product.

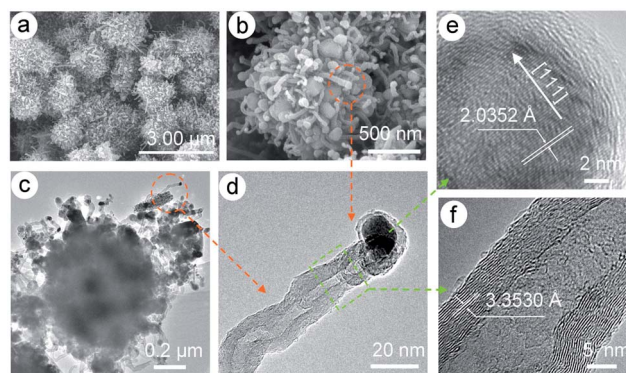


Fig. 3 (a) Slightly enlarged SEM image of a typical product. (b) SEM and (c) TEM images of a typical rambutan-like particle. (d) TEM image of a typical MWCNT with catalyst particle encapsulated at the tip. The HRTEM images of (e) the catalyst particle and (f) the MWCNT.

300 to 500 nm tortuous wires growing radially from the core. The TEM image in Fig. 3d revealed that the wire was practically crooked or twisted MWCNT with an inner diameter of about 5 to 10 nm and tube-wall thickness of about 8 nm. An irregular nanoparticle of about 20 nm was typically found to locate at the CNT tip. The top surface was covered with some amorphous C molecules and the bottom was connected with ordered sp^2 C. In the HRTEM image of the catalyst particle (Fig. 3e), the 2.0352 Å spacing between neighboring lattice planes corresponded to the distance between the (111) Ni planes. This data demonstrated that C diffusion was along the surface of Ni-catalyst particles. The HRTEM image of a CNT (Fig. 3f) showed that the CNTs were multiwalled and consisted of about 25 graphite layers with 3.3530 Å interplanar spacing. Therefore, our product was composed of Ni cores coated with MWCNT-containing Ni-catalyst particles.

No carbide phase detected by XRD and TEM further demonstrated that the MWCNT formation in this study was not triggered by an intermediate Ni carbide phase (Ni_3C);²⁶ in other words, the MWCNT growth was monitored by metallic Ni located on its tip as the active catalyst. Apparently, the aforementioned growth process followed a tip-growth mode rather than a base-growth mode. Nevertheless, MWCNT formation in the present study involved the following steps: adsorption and decomposition of C precursor molecules on the particular faces of Ni catalyst, and atomic C diffusion and its transformation into a tubular structure around the particles. Furthermore, Ni nanoparticles were used as a catalyst for the formation of SWCNTs,²⁷ MWCNTs,²⁸ C nanospheres, and graphite nanofibers.²⁹ Many studies have shown that the surface orientation, shape, and size of Ni particles significantly affect the CNT type and structure.³⁰ For example, the growth mode changes from tip growth (for large particles, $\gg 5\text{ nm}$) to base growth (for small particles, $< 5\text{ nm}$). SWCNTs and MWCNTs with few walls (typically < 7 walls) grow from their base, whereas larger MWCNTs are fed with C through their tips that support the catalyst particle.³¹ According to the proposed catalytic growth mechanism, crooked, twisted, or helical MWCNTs may result from

variations in C segregation, catalyst geometry, or catalytic activity on the active sites (around the catalyst periphery) during nanotube growth.³²

Formation mechanism

An attempt to reveal the assembly mechanism of rambutan-like Ni/MWCNT heterostructures was made using time-dependent experiments. SEM, TEM, and XRD were used to check the morphology, microstructure, and crystal phase evolution of the intermediate products obtained at various stages of a typical synthesis, respectively.

As decomposition started, *ca.* 1.0 μm octahedral NiO precursors (Fig. 4a and 5) transformed into nanoparticle-built aggregates only at 0.5 h of reaction time (Fig. 4b and 5). The corresponding TEM image confirmed that C films about 10 to 30 nm thick were coated on the aggregate surface and some small Ni nanoparticles encapsulated by C films began to separate from the aggregate surface (Fig. 4c). When *t* reached 1 h, a small quantity of short MWCNTs, 100 to 200 nm long and 20 nm in diameter, grew out of the aggregate surfaces, thereby forming rambutan-like Ni/MWCNT heterostructures about 1.5 μm in diameter (Fig. 4d and e). The XRD data in Fig. 5 show that hexagonal graphite peaks were strengthened with prolonged *t*, indicating higher graphitization and/or content. Further prolonged *t* (up to 4 h) yielded larger spherical aggregates coated by longer and denser MWCNTs (Fig. 4f). Length of MWCNTs is about 1–2 μm . EDX analysis of these products revealed that C mass fractions in the obtained Ni/MWCNT composites increased from 32.55% at *t* = 0.5 h to 79.38% at *t* = 2 h. In fact, the *t* dependence of morphology and composition provided evidence that changing *t* can effectively adjust the length and density of MWCNTs.³³

Based on the above discussion, a possible formation mechanism was proposed and is illustrated in Fig. 6. The reactions during the process can be written as follows.³⁴

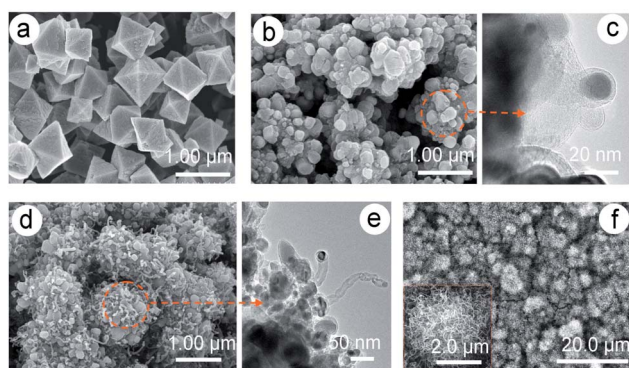
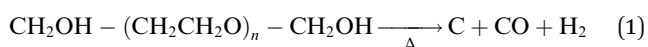


Fig. 4 (a) SEM images of octahedral NiO precursors. (b, d, and f) SEM images and (c and e) TEM images of the products obtained with δ = 20 at 750 $^{\circ}\text{C}$ for the following *t*: (b and c) 0.5 h, (d and e) 1 h, and (f) 4 h.

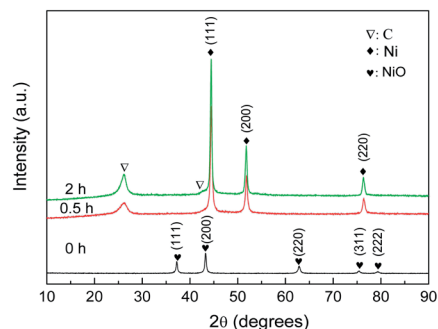


Fig. 5 XRD patterns of the products produced at 750 $^{\circ}\text{C}$ at various time points.



At the initial stage, as the C source of the process, organic molecules (*i.e.*, PEG 20 000) were adsorbed onto the octahedral NiO particle surface and then decomposed to generate C atoms and/or clusters, with the production of CO and H₂ [Fig. 6①]. Together with H₂ and CO, some carbons reduced NiO into Ni nanoparticles, and others were covered on its external surface to form the Ni/C film core-shell structure [Fig. 6② and ③]. Ni nanoparticle encapsulated with C films hindered Ni particle growth, resulting in the formation of nanoparticle-built aggregates [Fig. 6④].

Due to the weak interaction between Ni catalyst and NiO aggregates, C diffused down the (111) surface of Ni particles, and MWCNTs precipitated outside the metal bottom to push the whole Ni nanoparticle off the aggregates [as depicted in Fig. 6⑤]. Consequently, the rambutan-like Ni/MWCNT heterostructures formed. If the top of Ni catalyst was open for fresh hydrocarbon decomposition, MWCNTs continued to elongate.³⁵ Therefore, further prolonged *t* led to the formation of heterostructures with more uniform, longer, denser MWCNTs [Fig. 6⑥ and ⑦]. During the above catalytic decomposition, the formed amorphous C was subsequently graphitized by interaction with the catalyst. In the absence of a catalyst, amorphous C generally transformed into graphite at the high temperature (from 2500 to 3500 $^{\circ}\text{C}$). When Ni catalyst presented, the above transformation occurred at a relatively low temperature (*i.e.*, 600 to 900 $^{\circ}\text{C}$). The Ni catalytic activity ceased and MWCNT growth stopped until the metal was fully covered with excess C. The formation of MWCNTs containing Ni catalyst particles at the tip can be ascribed to the catalysis of some small Ni nanoparticles detached from the Ni cores. This formation process possibly followed a tip-growth mode.³⁶ The above carbon-based heterostructures may have formed similarly as the hollow Ni sphere composites covered with CNTs¹⁵ and composites of Co/CNTs.¹³ The CNTs all grew from the Co flower surface that had contact with the C source, which was believed to follow a bottom-growth mode.¹³

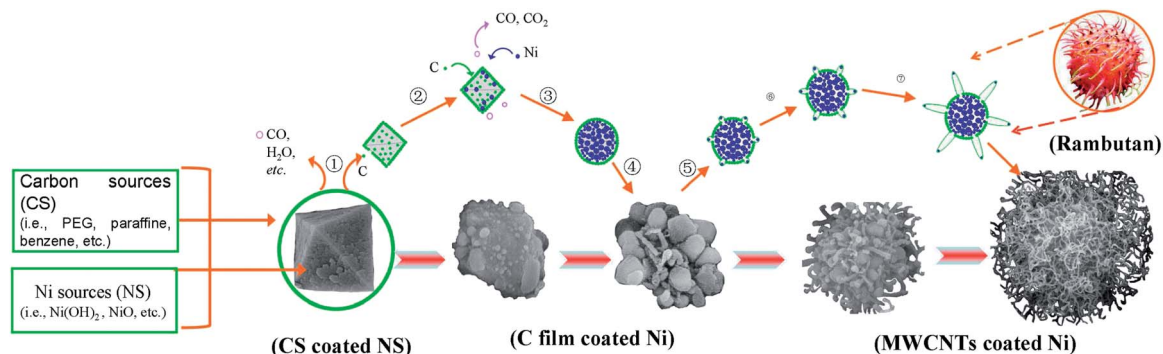


Fig. 6 Schematic of the formation of rambutan-like Ni/MWCNT heterostructures.

Influences of reaction conditions

According to the normal mechanism, three key factors were required for Ni/MWCNT composite formation: the feeding ratio of C source to Ni source, the C source, and the type of Ni precursor. We systematically investigated the influence of reaction conditions on the morphology and composition of products. As shown in the SEM and EDX data (Fig. 7), the PEG 20 000 to NiO mass ratio can also be used to modulate the morphology and composition of the products. Only particle-based aggregates were obtained at $\delta = 3$, covered with several nanometers of C film in a low mass fraction of 9.9% (Fig. 7a and b). Increasing δ to 7.5 caused the formation of uniform rambutan-like architectures of 1 to 2 μm in size coated by numerous 300 to 500 nm tortuous CNTs (Fig. 3). By contrast, the products formed at $\delta = 50$ were larger spherical aggregates of *ca.* 4 to 5 μm surrounded by longer and denser CNTs with length of about 2 μm and a high mass fraction of 86.3% (Fig. 7c and d). Apparently, increased δ induced the change from C films to CNTs, as well as the enhancement of C mass fraction and MWCNT length. Therefore, changing δ can easily modulate both the morphology and composition of products.

Apart from the PEG 20 000 to NiO mass ratio, the type of C source and Ni precursor also crucially affected the morphology

and composition of the products. The most commonly used CNT precursors are CH_4 , CO ,³⁷ C_2H_2 ,³⁸ C_2H_4 ,^{39,40} benzene,⁴¹ and xylene.⁴² In this study, various types of organic matter such as PEG 400, benzene, and paraffin were chosen. Substituting PEG 20 000 with other C sources (*e.g.*, PEG 400, paraffin, and benzene) can also yield rambutan-like Ni/MWCNT heterostructures. Due to the low content, weaker C-diffractive peaks were exhibited by the products formed by paraffin pyrolysis than those formed using PEG 400 and benzene as C sources (Fig. 8a). SEM and EDX data further confirmed the above results. When paraffin served as C sources, only short and sparse MWCNTs grew on the surface of the aggregates (1 μm diameter), with low C mass fraction of 11.94% (Fig. 8b). If using PEG 400 as the C source, *ca.* 2 μm aggregates can be observed, coated by thicker and longer MWCNTs (Fig. 8c). The C mass fraction was 75.39%. Furthermore, using benzene as the C source yielded fluffy, spherical aggregates (5 μm in size) coated by denser and longer CNTs in a high C mass fraction of 92.98% (Fig. 8d).

This study proved that the C source played crucial roles in CNT growth. First, the standard heat of enthalpy affected the initial growth rate and burning rate of CNTs. These oxidant

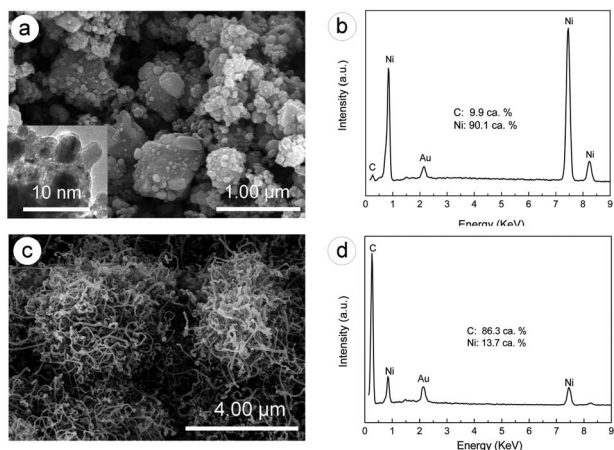


Fig. 7 (a and c) SEM images and (b and d) EDX patterns of the products formed at 750 °C under N_2 with various δ of (a and b) 3 and (c and d) 50.

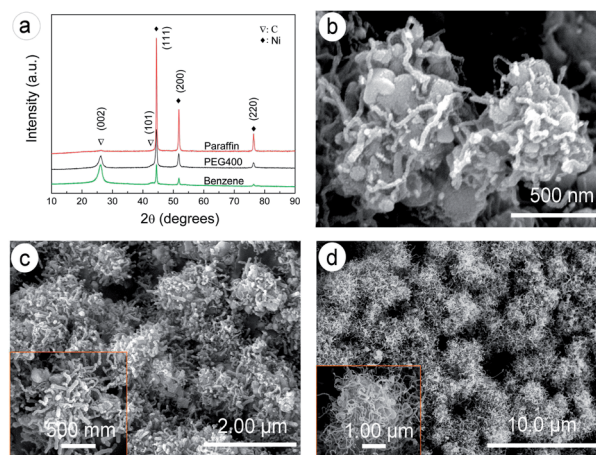


Fig. 8 (a) XRD patterns and (b and c) SEM images of the products formed with different C sources at 750 °C of (b) PEG 400, (c) paraffin, and (d) benzene.

species and activated C sources were more easily generated from the C sources having a low absolute value of enthalpy than those having a high one. Nakatsuka⁴³ found that a higher molecule number of C sources led to lower initial growth rate of CNTs. Second, the C content in the C sources was more directly associated with the composition and morphology of the products. Third, the C source molecular structure crucially affected the morphology of grown CNTs. Linear hydrocarbons such as methane, ethylene, and acetylene thermally decomposed into atomic carbons or linear dimers/trimers of C and generally produced straight, hollow CNTs. Meanwhile, cyclic hydrocarbons such as benzene, xylene, cyclohexane, and fullerene produced relatively curved or hunched CNTs with tube walls often bridged inside.^{44,45} In this study, PEG 400 with fewer molecules than paraffin had a higher initial growth rate of CNTs. Benzene had a higher C content than other C sources, indicating that growth kinetics depended on the C sources. Choice of such materials will open a new way in the formation of carbonaceous structures.

In addition, substitutions of octahedral NiO precursors with spherical Ni(OH)₂ and rod-like NiO can also form rambutan-like Ni/MWCNTs composites (see the ESI S1†). For example, hollow Ni/MWCNT rambutan-like composites (2 to 30 μm in size) were produced using hollow spherical Ni(OH)₂ as the Ni source and catalyst (Fig. S1a–c†). The C mass fraction was 72.85%. By contrast, the products using NiO nanorods were rambutan-like Ni/MWCNT composites 1 to 2 μm in size with a C mass fraction of 59.85% (Fig. S1d†). The generality of the current CVD method for the synthesis of rambutan-like Ni/MWCNTs heterostructures was confirmed in this study. This method can be extended to the synthesis of other MWCNT-based heterostructures. The corresponding work is ongoing.

Static magnetic properties

The magnetic properties of the Ni/MWCNT samples were studied at room temperature using a vibrating sample

magnetometer. As shown in Fig. 9, all samples exhibited typical ferromagnetic hysteresis curves that reached saturation below 2.5 kOe magnetic field. Saturation magnetization (M_s) gradually decreased with increased δ from 41.07 emu g^{−1} (at $\delta = 3$) to 22.72 emu g^{−1} (at $\delta = 7.5$) and even to 11.02 emu g^{−1} (at $\delta = 15$). Apparently, the above values were lower than that of bulk nickel (*ca.* 55.15 emu g^{−1}). Some factors such as impurities, specific morphology,⁴⁶ surface antiferromagnetic oxidation, surface spin disorder, grain size,⁴⁷ crystallinity,⁴⁸ superexchange interactions, nanoeffects, and magnetic interactions are generally responsible for M_s variation.⁴⁹ In this study, the decreased M_s may be related to the special flower-shaped heterostructures consisting of the ferromagnetic Ni core and diamagnetic MWCNT shell. In general, graphite is diamagnetic, with -21.5×10^{-6} emu g^{−1} parallel to the magnetic field and -0.5×10^{-6} emu g^{−1} perpendicular to the magnetic field.⁵⁰ Therefore, the existence of massive MWCNTs causes the declined M_s . As the δ increased, the mass fraction of nonmagnetic MWCNTs also increased from 9.9% at $\delta = 3.0$, to 33.67% at $\delta = 7.5$, to 78.7% at $\delta = 15$, resulting in gradually declined M_s . Similar behaviors have been observed in previous works.⁵¹

The H_c values varied in small ranges: 174.88 Oe (at $\delta = 3$), 178.9 Oe (at $\delta = 7.5$), and 164.99 Oe (at $\delta = 15$). These values were significantly higher than those of bulk Ni (*ca.* 0.7 Oe),⁵² prickly Ni chains (88.91 Oe),⁵³ hierarchical Ni microstructures (121 Oe),⁵⁴ Ni octahedra (131.85 Oe),⁴⁸ and spherical Ni nanoparticles (40 Oe).⁵⁵ The magnetic material coercivity generally originated from various anisotropy types, including crystal, shape, stress, externally induced, and exchange anisotropy. In the present research, the enhanced coercivity may be related to the specific rambutan-like heterostructure, leading to a combination of the coupling and spatial confinement effect. Similar results can also be observed in other flower-like structures. This finding indicated that the magnetic properties of the Ni/MWCNT samples can be easily manipulated through the morphology and composition of the products.

Microwave EM properties

Fig. 10a–c shows the complex permittivity and dielectric loss of wax composites containing 30% mass fraction of the samples obtained at different δ . ϵ' , ϵ'' , and $\tan \delta_E$ increased as δ varied from 3.0 to 15. This indicates that the rambutan-like Ni/MWCNT heterostructures with high C mass fraction and/or long MWCNTs possess higher storage and loss capabilities for electric energy compared with Ni/C film core-shell structures. With frequency increasing from 2 to 18 GHz, the values of ϵ' , ϵ'' , and $\tan \delta_E$ edged down slowly from $\delta = 3.0$ to $\delta = 7.5$ and drastically at $\delta = 15$. In terms of the loss mechanism, the dielectric loss can be classified by conductance loss ($t_g\delta_c$), dielectric relaxation loss ($t_g\delta_{rel}$), resonance loss ($t_g\delta_{res}$), and so on, strongly depending on size, morphology, composition, conductivity, polarization model and so forth. On the one hand, the enhanced dielectric characteristics of Ni/MWCNT heterostructures are attributed to their special morphologies. Such radial nanostructures can generate special orientation and interface polarizations, causing enhanced dielectric losses. On

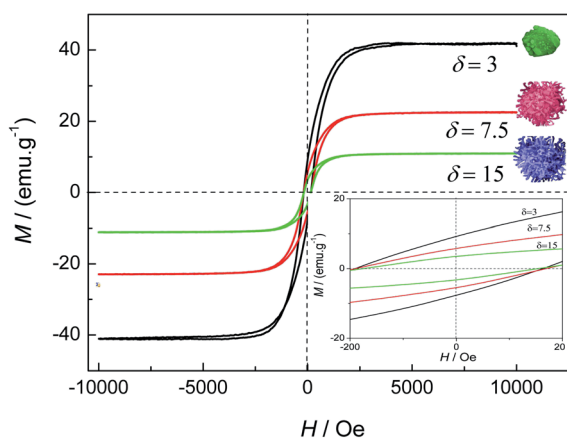


Fig. 9 Magnetic hysteresis loops of the samples obtained by reducing the NiO precursors at different mass ratios of PEG 20 000 to NiO (δ). The lower-right inset is the magnified hysteresis loops at the low applied fields.

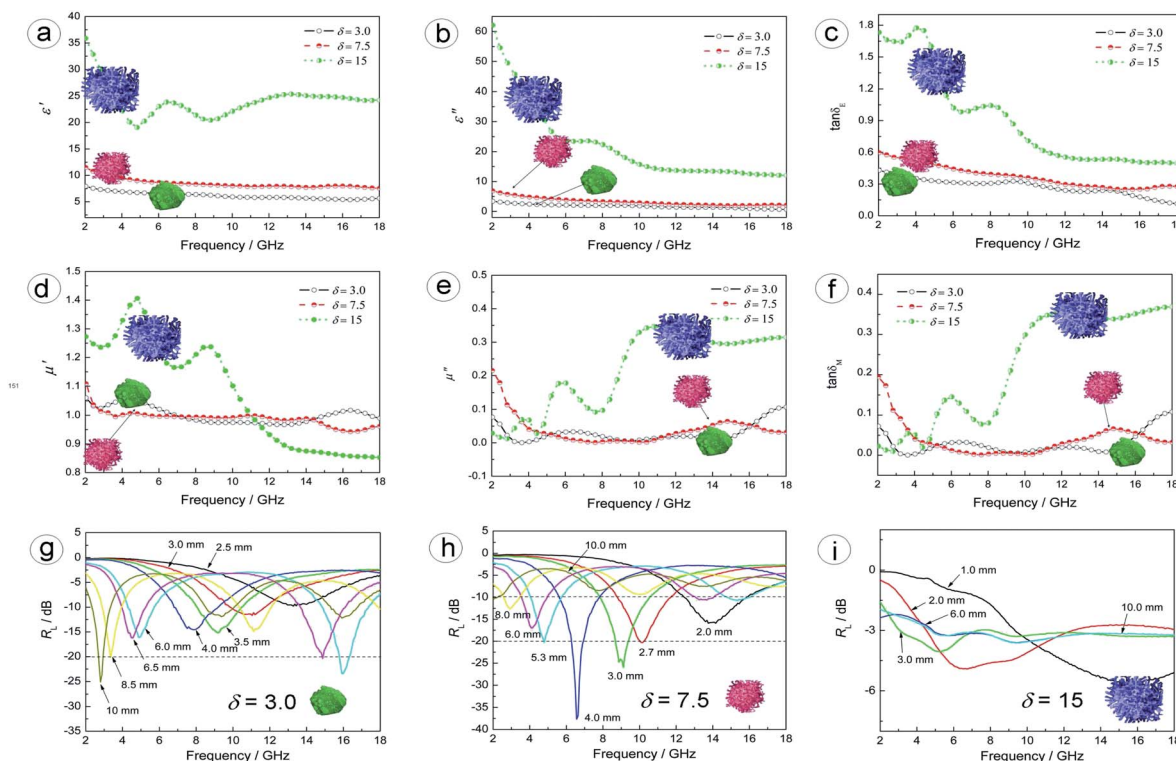


Fig. 10 Frequency dependence of (a–f) electromagnetic parameters and (g–i) reflection loss curves (R_L) of wax composites containing 30% mass fractions of the samples obtained at different mass ratios of PEG 20 000 to NiO (δ). (a) Real (ϵ') and (b) imaginary (ϵ'') parts of the complex permittivity, (c) dielectric loss ($\tan \delta_E$), (d) real (μ') and (e) imaginary (μ'') parts of the complex permeability, (f) magnetic loss ($\tan \delta_M$).

the other hand, from the equation $t_g \delta_c = 1.8 \times 10^{10} \sigma / f \epsilon_r$,¹ it can be seen that the dielectric loss increases with σ and gradually decreases with f . As for Ni/MWCNT heterostructures, Ni is a dual loss matter with magnetic loss and dielectric loss, whereas MWCNTs are dielectric loss materials with high conductivity (σ). So Ni/MWCNT heterostructures with long MWCNTs and high MWCNT mass fraction have large conductance loss, showing a downward trend with f . Also, the eddy current loss induced by EM waves increases with increased f , resulting in the fall trend. A steep increase in ϵ' , ϵ'' , and $\tan \delta_E$ at $\delta = 15$ may be related to the conductive percolation network formation in the matrix.¹ The phenomenon is usually found in a high mass fraction, or one-dimension or flower-shaped lightweight nano-materials. Using the samples obtained at $\delta = 7.5$ as absorbent, the percolation semiconductive network can form at a mass fraction of 50% (see the ESI S2†). This demonstrates that increasing C mass fraction and/or MWCNT length facilitates the formation of the percolation semiconductive network in a low mass fraction. Our data indicate that the dielectric properties could be easily tuned by changing C mass fraction and/or MWCNT length of the rambutan-like Ni/MWCNT heterostructures.

Fig. 10d–f reveal the complex permeability and magnetic loss of wax composites containing 30% mass fractions of the samples obtained at different δ . At $\delta = 3.0$ and 7.5, the values of μ' , μ'' , and $\tan \delta_M$ fluctuated within a narrow range without sharp distinction. When the δ increased to 15, μ' took on a

downward trend, while μ'' and $\tan \delta_M$ showed a steep uptrend with frequency. This indicated that enhanced μ'' and $\tan \delta_M$ can be displayed by rambutan-like Ni/MWCNT heterostructures with long MWCNTs or high C mass fraction. Generally, the microwave magnetic loss mostly originates from magnetic hysteresis, domain wall resonance, eddy current loss, natural resonance, and exchange resonance. Therefore, magnetic hysteresis from irreversible magnetization only takes place in a strong applied field, whereas domain wall resonance from multidomain materials only occurs in the low frequency range (<2 GHz). Thus, the permeability of the obtained heterostructures is mainly due to eddy current loss, natural resonance, and exchange resonance rather than magnetic hysteresis or domain wall resonance.

According to the equation $\mu''(\mu')^{-2}f^{-1} = \frac{2}{3}\pi\mu_0 d^2 \sigma$,⁴⁶ where μ_0 is vacuum permeability, d is the thickness, and σ is the electric conductivity, if the magnetic loss only stems from the eddy current loss, the values of $\mu''(\mu')^{-2}f^{-1}$ should be constant as frequency increases. The values of $\mu''(\mu')^{-2}f^{-1}$ of the samples obtained at $\delta = 3.0$ and 7.5 were similar at 5–18 GHz (Fig. 11). This means that the eddy current loss greatly contributed to μ'' and magnetic loss over this frequency range. Two sharp resonance peaks at 5–8 GHz and 8–15 GHz were observed in the $\mu''(\mu')^{-2}f^{-1}$ plot of rambutan-like Ni/MWCNT heterostructures with long MWCNTs obtained at $\delta = 15$. This suggests that the enhanced μ'' and $\tan \delta_M$ for the samples formed at $\delta = 15$ were chiefly caused by natural resonance and exchange resonance.

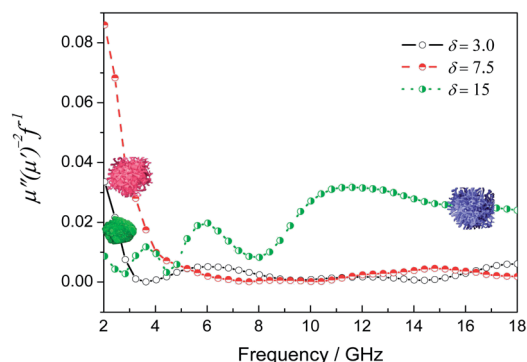


Fig. 11 Plots of $\mu''(\mu')^{-2}f^{-1}$ for the samples produced at various δ .

Some multiresonant peaks occurred on the plots of μ'' and $\tan \delta_M$ and significantly strengthened at $\delta = 15$. Owing to the capacitance lead or lag behind an angle of 90° compared with the inductance, the change trend of permeability resonance is contrary to that of permittivity resonance. These multiresonant behaviors may be related to special flower-shaped heterostructures consisting of ferromagnetic Ni core and diamagnetic MWCNT shell. Ni ferromagnetic resonance contained two parts: the uniform-precession mode and non-uniform-precession or spin-wave modes. The former is also known as natural resonance and usually appears at a relatively low frequency; the latter is called exchange resonance and always emerges at a higher frequency, which is usually related to small size effect, surface effect, and spin wave excitations. MWCNTs are high-dielectric loss matter. Thus, the recombination of MWCNTs with Ni may generate multiresonance phenomena because of highly conductive and skin effects, electronic spin and charge polarizations caused by point effects, as well as polarized centers. Similar multiresonance behaviors have been found in CNT/Fe powder composites,¹ Fe/expanded graphite intercalation compounds,⁵⁶ and steel slag-charcoal composite.⁵⁷ This further demonstrates that the multi-resonance behavior of the ferromagnetic material is sensitive to its morphology and composition.

Based on the above EM parameters at the given f and d , the reflection loss (R_L) representing the material-absorbing ability is usually calculated according to the transmission line theory.

$$R_L(\text{dB}) = 20 \log_{10} |(Z_{\text{in}} - Z_0)/(Z_{\text{in}} + Z_0)| \quad (4)$$

$$Z_{\text{in}} = Z_0 \sqrt{\mu/\epsilon} \tanh \left[j(2\pi f d/c) \sqrt{\mu/\epsilon} \right] \quad (5)$$

$$Z_0 = \sqrt{\mu_0/\epsilon_0} \quad (6)$$

Fig. 10g–i shows the R_L curves of wax composites containing 30% mass fractions of the samples obtained at different δ . All R_L curves were found to gradually shift to lower frequencies with the increased d . Each R_L curve reached minimum values when the coating thickness (d_m) and frequency (f_m) satisfied the matching relationship $d_m = c / (4f_m \sqrt{|\mu||\epsilon|})$. For the Ni/C film core-shell structures formed at $\delta = 3$, a minimum R_L value of

−24.9 dB appeared at 2.8 GHz, corresponding to 10.0 mm matching thickness (Fig. 10g). R_L values were almost under −10 dB at the whole frequency of 2–18 GHz. The Ni/MWCNT heterostructures with short MWCNTs obtained at $\delta = 7.5$ show an optimal microwave absorption property. The minimum R_L value of −37.9 dB occurred at 6.5 GHz on a coating with a 4.0 mm matching thickness (Fig. 10i). In particular, the absorption range at −20 dB was from 4.7 to 10.2 GHz, which corresponds to 2.7–5.3 mm matching thicknesses. Notably, the above values ($R_L \leq -20$ dB) of 5.5 GHz was broader than those reported in literature (*i.e.*, carbon-coated Ni nanocapsules (1.0 GHz)⁵⁸ and Ni nanowires (0 GHz)⁵⁹). By comparison, the Ni/MWCNT heterostructures with long MWCNTs obtained at $\delta = 15$ show the weak absorption ability with R_L values over −10 dB at the whole frequency of 2 to 18 GHz (Fig. 10h). According to the matching and attenuating characteristics, EM parameters from the ideal absorption coating must meet the equation $\mu \approx \epsilon$ in a wide frequency range and the dielectric loss and magnetic loss are as large as possible. Obviously, the matching and attenuating characteristics of the samples decreased and increased with increasing δ , respectively. In this case, optimal matching and attenuating characteristics were available for the rambutan-like Ni/MWCNT heterostructures formed at $\delta = 7.5$. Besides that, the improved electromagnetic characteristics are usually ascribed to rambutan-like Ni/MWCNT heterostructures, generating special dielectric relaxation, microcurrent attenuation, interface scattering, and microantenna radiation.⁶⁰

Conclusions

A universal approach has been developed for the selective synthesis of rambutan-like Ni/MWCNT heterostructures through the one-pot decomposition of organic matter and Ni precursor mixture under Ar. Research on the reaction process revealed the formation mechanism in which MWCNTs capped by Ni nanoparticles grew on the surface of Ni nanoparticle-built spheres following a tip-growth mode. Some dynamic factors including time, mass ratio of PEG 20 000 to NiO, as well as type of C source and Ni precursor can be easily used to adjust the composition and morphology of the rambutan-like heterostructure. As the δ increases from 3.0 to 15, the C mass fraction increased and the sample morphology varied from Ni/C film core-shell structures to rambutan-like Ni/MWCNT heterostructures. Such changes resulted in the decreased M_s and enhanced permittivity properties with δ . Due to intensive eddy current loss and multiresonance behaviors, significantly improved complex permeability was exhibited by rambutan-like Ni/MWCNT heterostructure with long MWCNTs formed at $\delta = 15$; an optimal microwave absorption property with a minimum R_L value of −37.9 dB occurring at 12.8 GHz can be observed for Ni/MWCNT heterostructures coated by short MWCNTs formed at $\delta = 7.5$. In particular, the absorption range under −20 dB was over 5.0 to 9.2 GHz. The current work provides insights into the absorption mechanism of rambutan-like heterostructure absorbers. CNT-based hybrid structures with desired compositions and/or morphologies can modulate the properties of materials and find potential applications in biomedicine,

photocatalysis, electrode material, microwave absorption, and nanodevices.

Acknowledgements

This work is financially supported by the National Natural Scientific Foundation of China (51102215), Chinese Scholarship Council (201208330114), Natural Scientific Foundation of Zhejiang Province (Y14B010003), Teacher Training Project of Zhejiang Normal University (KYJ06Y12134), and National Innovation and Entrepreneurship Training Program of Undergraduates (201310345016).

References

- G. X. Tong, W. H. Wu, Q. Hua, Y. Q. Miao, J. G. Guan and H. S. Qian, *J. Alloys Compd.*, 2011, **509**, 451.
- H. S. Kim, H. Lee, K. S. Han, J. H. Kim, M. S. Song, M. S. Park, J. Y. Lee and J. K. Kang, *J. Phys. Chem. B*, 2005, **109**, 8983.
- G. P. Jin, Y. F. Ding and P. P. Zheng, *J. Power Sources*, 2007, **166**, 80.
- Y. Cho, G. Choi and D. Kim, *Electrochem. Solid-State Lett.*, 2006, **9**, 107.
- M. Horton, H. P. Hong, L. Chen, B. Shi, G. P. Peterson and S. H. Jin, *J. Appl. Phys.*, 2010, **107**, 104320.
- C. Soldano, F. Rossella, V. Bellani, S. Giudicatti and S. Kar, *ACS Nano*, 2010, **4**, 6573.
- X. C. Gui, W. Ye, J. Q. Wei, K. L. Wang, R. T. Lv, H. W. Zhu, F. Y. Kang, J. L. Gu and D. H. Wu, *J. Phys. D: Appl. Phys.*, 2009, **42**, 075002.
- Q. Xu, L. Zhang and J. Zhu, *J. Phys. Chem. B*, 2003, **107**, 8294.
- R. T. Lv, F. Y. Kang, W. X. Wang, J. Q. Wei, J. L. Gu, K. L. Wang and D. H. Wu, *Carbon*, 2007, **45**, 1433.
- R. Kozhuharova, M. Ritschel, D. Elefant, A. Graffl, I. Mönch, T. Mühl, C. M. Schneider and A. Leonhardt, *J. Magn. Magn. Mater.*, 2005, **290**, 250.
- K. R. Reddy, B. C. Sin, C. H. Yoo, W. J. Park, K. S. Ryu, J. S. Lee, D. Sohn and Y. Le, *Scr. Mater.*, 2008, **58**, 1010.
- H. Hou and D. H. Reneker, *Adv. Mater.*, 2004, **16**, 69.
- Z. Zheng, B. Xu, L. Huang, L. He and X. M. Ni, *Solid State Sci.*, 2008, **10**, 316.
- S. M. Zhang and H. C. Zeng, *Chem. Mater.*, 2009, **21**, 871.
- M. Han, W. L. Zhang, C. L. Gao, Y. Y. Liang, Z. Xu, J. M. Zhu and J. H. He, *Carbon*, 2006, **44**, 211.
- L. L. Zhang, Z. G. Xiong and X. S. Zhao, *ACS Nano*, 2010, **4**, 7030.
- U. Weissker, S. Hampel, A. Leonhardt and B. Büchner, *Materials*, 2010, **3**, 4387.
- G. X. Tong, Q. Hu, W. H. Wu, W. Li, H. S. Qian and Y. Liang, *J. Mater. Chem.*, 2012, **22**, 17494.
- A. Rinaldi, J. P. Tessonnier, M. E. Schuster, R. Blume, F. Girgsdies, Q. Zhang, T. Jacob, S. B. Hamid, D. S. Su and R. Schlögl, *Angew. Chem., Int. Ed.*, 2011, **50**, 3313.
- Y. J. Xiong, B. Wiley and Y. N. Xia, *Angew. Chem., Int. Ed.*, 2007, **46**, 7157.
- M. Audier, A. Oberlin and M. Coulon, *J. Cryst. Growth*, 1982, **57**, 524.
- J. Feng and H. C. Zeng, *J. Phys. Chem. B*, 2005, **109**, 17113.
- Q. L. Zhou, F. Gu and C. Z. Li, *J. Alloys Compd.*, 2009, **474**, 358.
- E. C. Vermisoglou, G. N. Karanikolos, G. Pilatos, E. Devlin, G. E. Romanos, C. M. Veziri and N. K. Kanellopoulos, *Adv. Mater.*, 2010, **22**, 473.
- H. Q. Hou, A. K. Schaper, F. Weller and A. Greiner, *Chem. Mater.*, 2002, **14**, 39904.
- T. Arie, H. Nishijima, S. Akita and Y. Nakayama, *J. Vac. Sci. Technol., B: Microelectron. Process. Phenom.*, 2000, **18**, 104.
- W. Q. Deng, X. Xin and W. Goddard, *Nano Lett.*, 2004, **4**, 2331.
- C. P. Deck and K. Vecchio, *Carbon*, 2005, **43**, 2608.
- F. Salman, C. Park and R. T. K. Baker, *Catal. Today*, 1999, **53**, 385.
- P. E. Anderson and N. M. Rodriguez, *J. Mater. Res.*, 1999, **14**, 2912.
- A. Gohier, C. P. Ewels, T. M. Minea and M. A. Djouadi, *Carbon*, 2008, **46**, 1331.
- Z. P. Huang, D. Z. Wang, J. G. Wen, M. Sennett, H. Gibson and Z. F. Ren, *Appl. Phys. A: Mater. Sci. Process.*, 2002, **74**, 387.
- K. Hernadi, A. Fonseca, J. B. Nagy, D. Bernaerts and A. A. Lucas, *Carbon*, 1996, **34**, 1249.
- J. P. Tessonnier and D. S. Su, *ChemSusChem*, 2011, **4**, 824.
- M. Kumar and Y. Ando, *J. Nanosci. Nanotechnol.*, 2010, **10**, 3739.
- M. Mertig, L. C. Ciacchi, R. Seidel and W. Pompe, *Nano Lett.*, 2002, **2**, 841.
- P. Chen, H. B. Zhang, G. D. Lin, Q. Hong and K. R. Tsm, *Carbon*, 1997, **35**, 1495.
- C. J. Lee, J. Park and J. A. Yu, *Chem. Phys. Lett.*, 2002, **360**, 250.
- G. Che, B. B. Lakshmi, C. R. Martin and E. R. Fisher, *Chem. Mater.*, 1998, **10**, 260.
- S. Fan, M. Chapline, N. Frankline, T. Tomblor, A. M. Cassel and H. Dai, *Science*, 1999, **283**, 512.
- R. Sen, A. Govindaraj and C. N. R. Rao, *Chem. Phys. Lett.*, 1997, **267**, 276.
- B. Q. Wei, R. Vajtai, Y. Jung, J. Ward, R. Zhang, G. Ramanath and P. M. Ajayan, *Nature*, 2002, **416**, 495.
- S. Oida, A. Sakai, O. Nakatsuka, M. Ogawa and S. Zaima, *Appl. Surf. Sci.*, 2008, **254**, 7697.
- O. A. Nerushev, S. Dittmar, R. E. Morjan, F. Rohmund and E. E. B. Campbell, *J. Appl. Phys.*, 2003, **93**, 4185.
- R. E. Morjan, O. A. Nerushev, M. Sveningsson, F. Rohmund, L. K. L. Falk and E. E. B. Campbell, *Appl. Phys. A*, 2004, **78**, 253.
- G. X. Tong, W. H. Wu, R. Qiao, J. H. Yuan, J. G. Guan and H. S. Qian, *J. Mater. Res.*, 2011, **26**, 1639.
- G. X. Tong, J. H. Yuan, J. Ma, J. G. Guan, W. H. Wua, L. C. Li and R. Qiao, *Mater. Chem. Phys.*, 2011, **129**, 1189.
- G. X. Tong, J. G. Guan, Z. D. Xiao, X. Huang and Y. Guan, *J. Nanopart. Res.*, 2010, **12**, 3025.
- G. X. Tong, M. Hong, J. G. Guan, J. H. Yuan, W. H. Wu and H. S. Qian, *Micro Nano Lett.*, 2011, **6**, 722.
- X. K. Wang, R. P. H. Chang, A. Parashinski and J. B. Kezerson, *J. Mater. Res.*, 1994, **9**, 1578.

- 51 G. X. Tong, W. Wan, J. G. Guan and Q. J. Zhang, *J. Inorg. Mater.*, 2006, **21**, 1461.
- 52 F. L. Jia, L. Z. Zhang, X. Y. Shang and Y. Yang, *Adv. Mater.*, 2008, **20**, 1050.
- 53 Z. G. An, S. L. Pan and J. J. Zhang, *J. Phys. Chem. C*, 2009, **113**, 1346.
- 54 G. B. Cheng, G. C. Wei, C. J. Hao and S. T. Li, *Electron. Mater. Lett.*, 2009, **5**, 123.
- 55 D. H. Chen and C. H. Hsieh, *J. Mater. Chem.*, 2002, **12**, 2412.
- 56 G. X. Tong, J. H. Yuan, J. Ma, M. Y. Qin, J. G. Guan and L. C. Li, *Sci. China: Chem.*, 2011, **41**, 1121.
- 57 G. X. Tong, J. H. Yuan, Q. Hua, M. Y. Qin, J. J. Cai and J. G. Guan, *J. Funct. Mater.*, 2011, **42**, 287.
- 58 X. F. Zhang, X. L. Dong, H. Huang, Y. Y. Liu, W. N. Wang, X. G. Zhu, B. Lv, J. P. Lei and C. G. Lee, *Appl. Phys. Lett.*, 2006, **89**, 053115.
- 59 B. Gao, L. Qiao, J. B. Wang, Q. F. Liu, F. S. Li, J. Feng and D. S. Xue, *J. Phys. D: Appl. Phys.*, 2008, **41**, 2.
- 60 (a) X. S. Fang, C. H. Ye, X. Ting, Z. Y. Wang, J. W. Zhao and L. D. Zhang, *Appl. Phys. Lett.*, 2006, **88**, 013101; (b) Q. Hu, G. X. Tong, W. H. Wu, F. T. Liu, H. S. Qian, J. G. Guan and D. Y. Hong, *CrystEngComm*, 2013, **15**, 1314; (c) G. X. Tong, W. H. Wu, Q. Hu, L. C. Li and J. P. Shen, *CrystEngComm*, 2012, **14**, 2071; (d) G. X. Tong, F. F. Du, L. J. Xiang, F. T. Liu, L. L. Mao and J. G. Guan, *Nanoscale*, 2014, **6**, 778.